Conformational Analysis of a Dermatan Sulfate-Derived Tetrasaccharide by NMR, Molecular Modeling, and Residual Dipolar Couplings

Alba Silipo,[a, b] Zhenqing Zhang,[c] F. Javier Cañada,[a] Antonio Molinaro,[b] Robert J. Linhardt,*[c] and Jesús Jiménez-Barbero*[a]

The solution conformation behavior of a dermatan-derived tetrasaccharide—ΔHexA-(1→3)-GalNAc4S-β-(1→4)-IdoA-α-(1→3)-red-GalNAc4S (S is a sulfate group)—has been explored by means of NMR spectroscopy, especially by NOE-based conformational analysis. The tetrasaccharide was present as four species, two of which are chemically different in the anomeric orientation of the reducing 2-deoxy-2-acetamido-galactose (red-GalNAc) residue, while the other two are the result of different conformations of the iduronic acid (IdoA) unit. The two α–β-interconverting anomers were present in a 0.6:1 ratio. Ring conformations have been defined by analysis of $^3J_{H,H}$ coupling constants and interresidual NOE contacts. Both 2-deoxy-2-acetamido-galactose (GalNAc) residues were found in the $^4C_1$ chair conformation, the unsaturated uronic acid (Δ-Hex A) adopts a strongly predominant half-chair $^1H_2$ conformation, while the IdoA residue exists either in the $^1C_4$ chair or in the $^2S_0$ skewed boat geometries, in a 4:1 ratio. There is a moderate flexibility of Φ and Ψ torsions as suggested by nuclear Overhauser effects (NOEs), molecular modeling (MM), and molecular dynamics (MD) studies. This was further investigated by residual dipolar couplings (RDCs). One-bond C–H RDCs ($^1D_{C,H}$) and long-range H–H ($^3D_{H,H}$) RDCs were measured for the tetrasaccharide in a phage solution and interpreted in combination with restrained MD simulation. The RDC-derived data substantially confirmed the validity of the conformer distribution resulting from the NOE-derived simulations, but allowed an improved definition of the conformational behavior of the oligosaccharides in solution. In summary, the data show a moderate flexibility of the four tetrasaccharide species at the central glycosidic linkage. Differences in the shapes of species with the IdoA in skew and in chair conformations and in the distribution of the sulfate groups have also been highlighted.

Introduction

The most abundant polysaccharides distributed throughout the human body are the glycosaminoglycans (GAGs). These unbranched and highly negatively charged molecules contain disaccharide repeating units consisting of 2-deoxy-2-acetamido-D-galactose (GalNAc) or 2-deoxy-2-acetamido-D-glucose (GlcNAc) and a uronic acid such as D-glucuronic acid (GlcA) or L-iduronic acid (IdoA). Hyaluronic acid, dermatan sulfate (DS), chondroitin sulfate (CS), heparin (Hp), heparan sulfate (HS), and keratan sulfate are members of this family, and with the exception of hyaluronic acid, these sulfated polysaccharides are covalently linked to core proteins, forming proteoglycans.[1] These molecules are located inside cells, on the cell surfaces, and in the extracellular matrixes of a wide variety of vertebrate and invertebrate tissues. Their locations and highly charged natures explain their roles in cell–cell and cell–matrix interactions in embryonic development, cell recognition, adhesion, and migration. Some GAGs (DS, CS, and HS) bind and regulate chemokines and growth factors.[2,3] The chemical natures of GAGs impart characteristic physical rheological properties, such as high viscosity and low compressibility, that make these molecules ideal as a lubricating fluids in the joints, and their rigidity lends structural integrity to cells and gives protection from mechanical damage, absorption, and distribution of compressive weight.[1–3]

DS and CS are related glycosaminoglycans composed of a disaccharide repeating unit of uronic acid (1→3)-linked to GalNAc. These disaccharide repeats are β-(1→4)-linked to one another to form polymers of DS or CS. Epimerization at the C-5 position of the uronic acid moiety during the biosynthesis of DS leads to mixtures of epimers of IdoA and GlcA. DS GAG is found mostly in skin, but also in blood vessels, the heart valves, tendons, and the lungs. Despite the wealth of data regarding the solution conformations of HP- and CS-derived oli-

[a] Dr. A. Silipo, Dr. F. J. Cañada, Prof. Dr. J. Jiménez-Barbero
Centro de Investigaciones Biològicas, CSIC
Ramiro de Maeztu 9,28040 Madrid (Spain)
E-mail: jjbarbero@cib.csic.es

[b] Dr. A. Silipo, Prof. Dr. A. Molinaro
Dipartimento di Chimica Organica e Biochimica
Università di Napoli "Federico II"
Complesso Universitario Monte S. Angelo, Via Cintia 4, 80126 Napoli (Italy)

[c] Dr. Z. Zhang, Prof. Dr. R. J. Linhardt
Departments of Chemistry and Chemical Biology, Biology, and Chemical
and Biological Engineering
Center for Biotechnology and Interdisciplinary Studies
Rensselaer Polytechnic Institute
Troy, NY 12180 (USA)
E-mail: linhar@rpi.edu

gosaccharides,[4–7] little or no information on the solution conformations of DS-derived oligosaccharides is available.[8] Glycosaminoglycan-degrading lyases (chondroitinase B and ABC) are able to cleave DS polymers through a β-elimination mechanism, producing a terminal uronate with a 4,5-double bond (ΔHexA) at the nonreducing end.[9] By this enzymatic treatment a DS-derived tetrasaccharide has been isolated and chemically characterized, and its NMR solution conformation has been assigned. The isolated tetrasaccharide has the following sequence:

HexA-(1→3)-GalNAc4S-α-(1→4)-IdoA-α-(1→3)-red-GalNAc4S
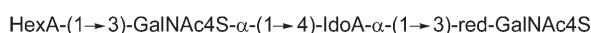
| A | B | C | D |

The conformational study of such GAG-derived oligo- and polysaccharides can be complicated by the well known conformational flexibility of the iduronic acid.[10–13] It has been reported that an internal IdoA residue can be present, depending on the substitution pattern, in $^4C_1$ chair and ^2S_O skewed boat ring conformations. Moreover, further complications derive from the presence of two interconverting α and β anomers at the reducing end and from the unsaturated uronate residue at the nonreducing end, which can exist in two half-chair conformations, $^2H_1$ and $^1H_2$.

The conformational behavior of a DS-derived tetrasaccharide has been explored by analysis of chemical shifts, NOEs, $^3J_{H,H}$ coupling constants, MM, and restrained MD calculations. The relative orientations of the sugar rings have been defined, starting with the interresidue NOE contacts, from which the interproton distances were deduced. MM calculations were performed, in order to provide an estimation of the energetically accessible conformational regions and to determine the low-energy regions centered around the Φ and Ψ glycosidic torsions. The conformational space available for the regions was then investigated by MD simulations. Restrained-MD simulations were carried out by use of the experimentally acquired NOE/J coupling information and the AMBER forcefield to obtain the best experimental conformer distributions of all the species in solution. The conformational behavior of the tetrasaccharide as suggested by NOE, MM, and MD studies has been further investigated by RDCs. One-bond C–H RCDs ($^1D_{C,H}$) and long range H–H ($^3D_{H,H}$) RCDs were measured for the tetrasaccharide in a phage solution. The TRAMITE (tracking alignment from the moment of inertia tensor)[14] method was used to align the MD trajectories and to back-calculate the average RDCs. Calculated RDCs were then compared with the experi-

mentally determined ones and interpreted with the assistance of MD simulations. These results were compared with those obtained from NOE-based information.

Results and Discussion

Isolation, purification, and characterization of dermatan sulfate tetrasaccharides

DS was partially digested with chondroitinase ABC. The percentage completion of digestion was quantified by dividing the UV absorbance (at 232 nm) of the products prepared with a given amount of enzyme for 10 h, by the UV absorbance at 232 nm determined at reaction completion. The absorbance at 232 nm indicated that the digestion was 50% complete. The digested product mixtures were separated by size on a Bio-Gel P10 column. Seven fractions were observed in the chromatography on Bio-Gel P10 (data not shown), containing disaccharide (degree of polymerization 2, dp2) to tetradecasaccharide (dp14). The molecular weight of each fraction was confirmed by electrospray ionization-mass spectrometry (ESI-MS, data not shown), by which molecular ions of the tetrasaccharide were observed at m/z 458.1 ([M−2H]$^{2-}$) and 918.1 ([M−H]). Further purification was based on semipreparative strong anion exchange high-performance liquid chromatography (SAX-HPLC). Analysis by analytical SAX-HPLC indicated that the purity of this tetrasaccharide after purification was > 97%. All signals observed in ESI-MS could be assigned to the dermatan sulfate tetrasaccharide.

NMR analysis

The monosaccharide spin systems were assigned by 1D and 2D NMR spectroscopy. The ^{1}H NMR spectrum is shown in Figure 1. A combination of homo- and heteronuclear 2D NMR experiment double quantum filtered COSY, TOCSY, transverse-
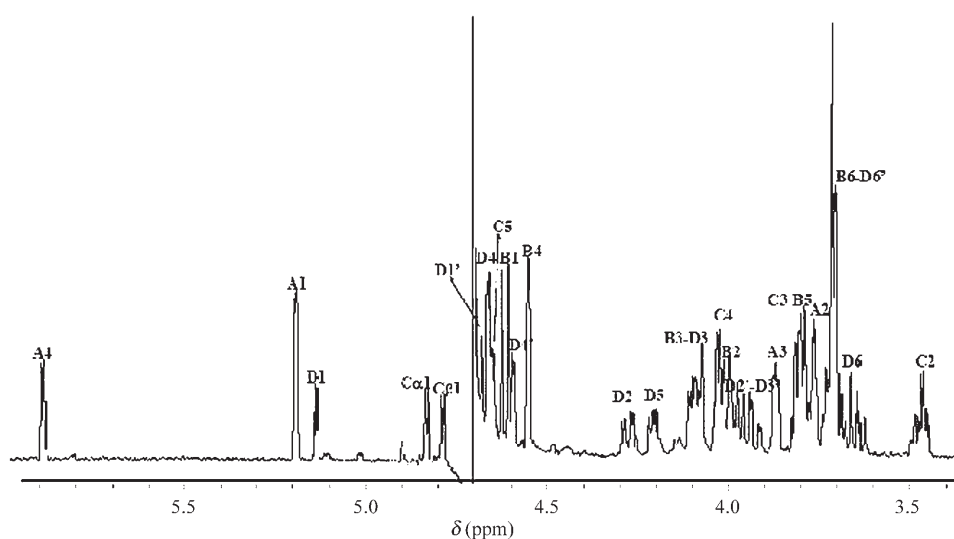
Figure 1. ^{1}H NMR spectrum (600 MHz, 298 K, pD 7.0) of the target dermatan-derived tetrasaccharide. Key NMR signals are indicated, denoted as indicated in Table 1.

Table 1. ^1H and ^{13}C (*italic*) NMR chemical shifts (δ, ppm) for the different sugar residues of the dermatan sulfate derived tetrasaccharide. Different values are observed for the GalNAcα (unit D) and -β (unit D′) anomers, and for their vicinal residues, dubbed as Cα and Cβ.

Unit	Chemical shift δ (^1H/^{13}C)					
	1	2	3	4	5	6
A	5.19	3.76	3.87	5.89	--	COOH
ΔHex-A	*99.9*	*68.4*	*64.4*	*106.47*		
D	5.19	4.28	4.09	4.66	4.20	3.65/3.70
α-*red*-GalNAc	*91.2*	*49.5*	*72.5*	*77.2*	*70.3*	*61.2*
		Ac *1.97/22.0*				
B	4.62	3.99	4.08	4.55	3.79	3.71
β-GalNAc	*102.0*	*51.9*	*75.5*	*76.0*	*74.5*	*60.9*
		Ac *2.04/22.4*				
D′	4.69	3.97	3.93	4.59	3.80	3.71
β-*red*-GalNAc	*94.8*	*53.0*	*75.3*	*76.1*	*74.5*	*60.9*
		Ac *1.97/22.0*				
C1β	4.79	3.47	3.80	4.02	4.66	COOH
IdoA (with β-*red*-GalNAc)	*103.2*	*69.5*	*71.6*	*80.7*	*69.7*	
C2α	4.83	3.46	3.82	4.03	4.66	COOH
IdoA (with α-*red*-GalNAc)	*102.9*	*69.5*	*71.6*	*80.7*	*69.7*	

ROESY, ^1H,^{13}C HSQC, and ^1H,^{13}C HMBC was executed in order to attribute all the spin systems. The proton resonances of all spin systems were obtained from the DQF-COSY and TOCSY spectra and were used to assign the carbon resonances in the HSQC spectrum. The anomeric configuration of each monosaccharide unit was assigned on the basis of the $^3J_{H1,H2}$ coupling constants obtained from the DQF-COSY and the intraresidual NOE contacts observable in the ROESY spectrum, whereas the values of the vicinal $^3J_{H,H}$ coupling constants allowed the identification of the relative configuration of each residue. In the anomeric region of the ^1H NMR spectrum (Figure 1) six signals (Table 1) for the tetrasaccharide ΔHexA-(1→3)-GalNAc4S-β-(1→4)-IdoA-α-(1→3)-*red*-GalNAc4S (residues **A**–**D**, respectively) were identified. Because of the presence of a free reducing end, represented by two residues **D** and **D′** (α- and β-GalNAc, respectively, Table 1), two signals were observed for the **D** residue. In addition, two different spin systems were identified for the IdoA residue **C**: **Cα** and **Cβ**, present in the α- and in the β-reducing form of the tetrasaccharide. The α and β anomers were present in a ratio of 0.6:1, as deduced from the relative integration of the ring proton signals of residues **D** and **D′** and of residue **B**.

Ring conformation and conformer population

Ring conformations have been defined by analysis of $^3J_{H,H}$ coupling constants obtained from one-dimensional ^1H NMR and two-dimensional DQF-COSY spectra and supported by analysis of the interresidual NOE contacts present in the ROESY spectrum.

Coupling constant values and intraresidue NOE contacts indicated that both GalNAc residues **B** and **D** were present exclusively in $^4C_1$ chair conformations, in which carbon atoms 4 and 1 are respectively above and below the plane defined by carbons 2, 3, and 5 and the intraring oxygen (O5).

The presence of a 4,5-double bond in the six-membered ring of residue **A** leads to a flattening of the chair due to the planar geometry of the double bond, generating the half-chair

conformation in which four contiguous carbons lie in one plane and the other two atoms lie on opposite sides of the plane. In principle, two almost isoenergetic half-chair conformations—$^2H_1$ and $^1H_2$—differing in the alternative above- and below-plane positions of C1 and C2, could exist for residue **A**; analysis of $^3J_{H,H}$ (Table 2) showed that the contribution to the

Table 2. Experimentally and theoretically determined coupling constant values (*J*, Hz) for the flexible pyranose residues C (IdoA) and A (ΔHexA). The experimentally determined values were estimated from high-resolution 1D NMR spectra at 600 MHz and in certain cases from highly resolved 2D double quantum filtered COSY. The theoretical values were obtained by applying the empirical Karplus equation proposed by Hassnoot et al. to the torsion angles derived from the MD simulations.

Experimentally and theoretically determined coupling constants				
	$^3J_{1,2}$	$^3J_{2,3}$	$^3J_{3,4}$	$^3J_{4,5}$
IdoA				
IdoA, C1 exp	3.8	8.4	7.6	3.1
IdoA, C2 exp	3.8	8.1	7.6	3.1
IdoA, $^4C_1$ calcd	2.0	2.1	2.0	3.4
IdoA, $^2S_0$ calcd	4.3	11.1	5.4	3.2
ΔHexA				
ΔHexA, A exp	2.9	ca. 1.3	4.8	–
ΔHexA, $^1H_2$ calcd	3.0	1.5	4.1	
ΔHexA, $^2H_1$ calcd	8.3	7.7	2.8	
ΔHexA: contribution of $^1H_2$ conformer: 100%, IdoA: $^2S_0$:$^4C_1$ ratio≅80:20				

equilibrium of the $^2H_1$ conformer is ca. 100%. The $^2H_1$ conformer is favored, as previously reported,[4–7,15] probably as the result of an intraresidual hydrogen bond between O1 and HO3.

Residues **B**, **D**, and **A** seemed to be almost conformationally rigid in solution. In contrast, coupling constants and NOE contacts demonstrated that residue **C** of IdoA was conformationally flexible. It has been reported[4–7] that IdoA residues can exist in both $^4C_1$ and $^1C_4$ chair conformations and also in a skew-boat $^2S_0$ conformation, and that their relative proportions vary as a function of the sugar sequence and of the attached sub-

© 2008 Wiley-VCH Verlag GmbH & Co. KGaA, Weinheim

stituents (if any). The contribution of each of these conformations was evaluated by analysis of $^3J_{H,H}$ values, which allowed us to exclude the presence of the $^4C_1$ form in equilibrium and to describe the two existing conformations as $^1C_4$ and $^2S_0$ (Table 2). The experimental data indicated that the equilibrium was significantly displaced toward the $^2S_0$ form (Table 2), the contribution of which was up to 80%, as reflected in the large $^3J_{H2,H3}$ and $^3J_{H3,H4}$ values. This was further confirmed by the strong and diagnostic NOE contact between H2 and H5 of residue **C**, which is only possible in the skew-boat $^2S_0$ conformation (Figure 2).

Vicinal $J_{5,6}$ coupling constants for the hydroxymethyl groups were also analyzed, and were in agreement with the typical *gt*:*tg* equilibrium of the ω torsion angles of a galactopyranose. Furthermore, analysis of the ROESY spectrum (Figure 2) gave evidence of remarkable NOE contacts of H1 and H2 **C** with the methyl protons of the *N*-acetyl group located on residue **D**, and of H1 and H2 **A** with the methyl protons of the *N*-acetyl group located on residue **B.**

In conclusion, the NMR data showed that the tetrasaccharide was present in the form of four different species differing in the anomeric orientation of the *red*-GalNAc unit and in the conformation of the IdoA unit. For abbreviation, these species are named as β-skew and α-skew (when the IdoA residue is present in the skew conformation with *red*-GalNAc as the β and the α anomer, respectively) and as β-chair and α-chair (when the IdoA residue is present in the chair conformation with the *red*-GalNAc as the β and the α anomer, respectively). The estimated relative abundances of these species, as inferred from the α/β anomer ratio and from the conformational equilibrium of the IdoA unit, were: β-skew 50%, α-skew 30%, β-chair 12.5%, and α-chair 7.5%.
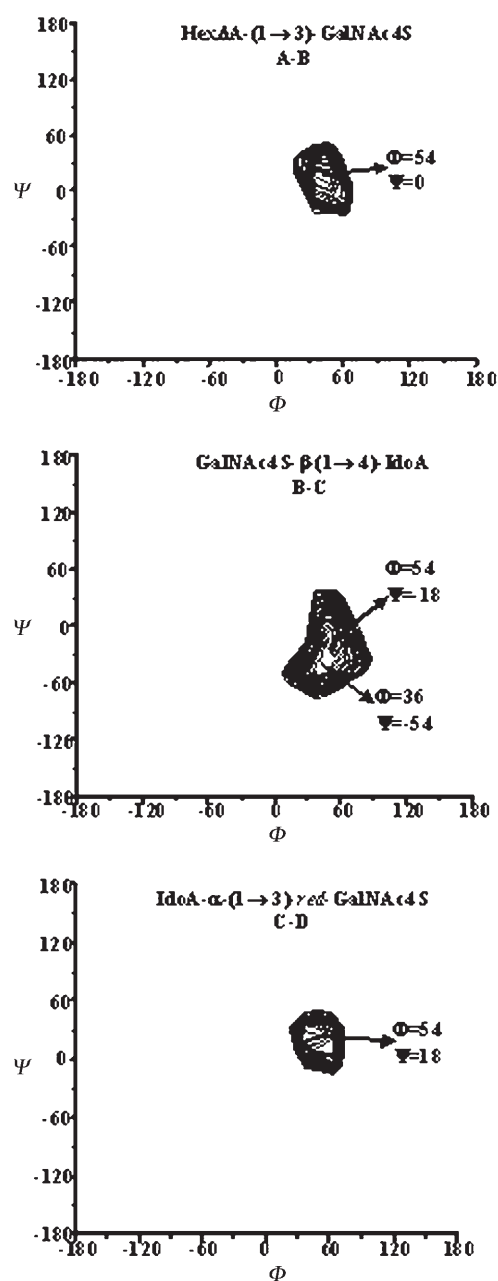
Molecular mechanics and molecular dynamics calculations

Since the conformation of an oligosaccharide is essentially defined by the relative orientations of the sugar moieties, and thus by *Φ* and *Ψ* glycosidic torsions, MM calculations have been performed to determine the best *Φ* and *Ψ* anomeric torsions and to provide a first estimate of the conformational regions energetically accessible. Only the results for the β-skew species are discussed here in detail, as no significant differences were found in the *Φ*/*Ψ* energy maps of all species. Indeed, the energy minima were found in the same region for each species.

The three disaccharides making up the dermatan sulfate tetrasaccharide—namely, **A**–**B** (ΔHexA-(1→3)-β-GalNAc4S, **B**–**C** (GalNAc4S-β-(1→ 4)-α-IdoA), and **C**–**D** (IdoA-α-(1→ 3)-β-GalNAc4S)—were constructed and subjected to extensive calculations with the AMBER* forcefield. Several maps were calculated, with account being taken of the two possible orientations of the ω torsion angle of the hydroxymethyl groups of both GalNAc residues and of the different orientations of the sulfate groups with respect to the sugar chain. One example of the resulting adiabatic energy maps is displayed in Figure 3 (in this case the *gt* conformer with the sulfate oriented equatorially with respect to the sugar moiety is reported). These *Φ*/*Ψ* surfaces provided a rough estimation of the conformational states that the disaccharide linkages could adopt. The glycosidic linkages all adopted *exo* anomeric[16] conformations; it could be observed that central disaccharide **B**–**C** is potentially more flexible, as the energy maps extend for a larger area (Figure 3), representing a higher number of conformational states. The lowest-energy regions of the **B**–**C** fragment were located around two energy minima: at $\Phi_{B–C}/\Psi_{B–C}$ 54/−18
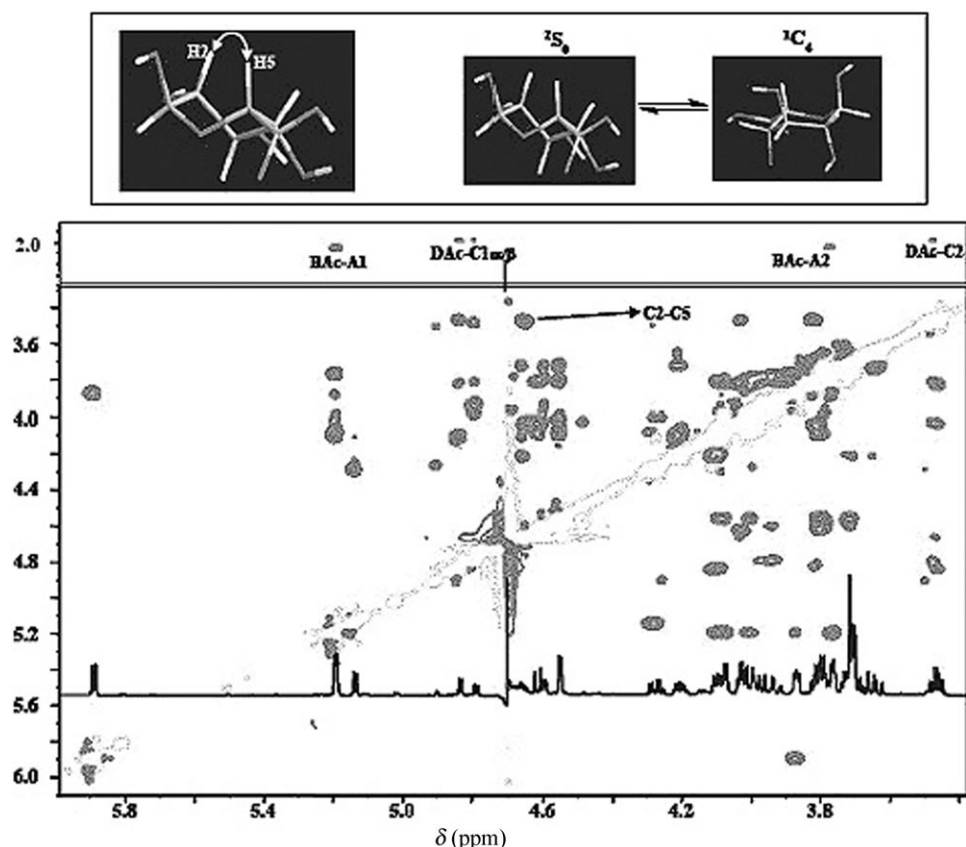
Figure 2. Key region of the 2D T-ROESY spectrum obtained with a 400 ms mixing time for the dermatan sulfate tetrasaccharide (600 MHz, 298 K, pD 7.0). Diagnostic and key NOE contacts are indicated. For instance, the strong C2–C5 cross peak indicated the presence of a high percentage of skew-boat conformers. The inset shows the equilibrium between the skew and the chair conformations of the IdoA residue.

Figure 3. Relaxed energy maps for the disaccharide fragments—ΔHexA-(1→3)-GalNAc4S, GalNAc4S-β-(1→4)-IdoA, and IdoA-α-(1→3)-*red*-GalNAc4S—that make up the target tetrasaccharide. Only those maps corresponding to the β-skew geometries of the IdoA ring are shown. Nevertheless, those for the α anomers or the chair conformers are very similar. The positions of the global and major local minima in the map are indicated.

Disaccharide portion	Φ	Ψ
HexA-GalNAc	54	0
GalNAc-IdoA	54	−18
	36	−54
IdoA-βGalNAc	54	18

and the $\Phi_{C–D}/\Psi_{C–D}$ glycosidic linkages are within the low-energy region around 54/18. Analogous optimal dihedral angles for all four disaccharide fragments species were found. Interestingly, neither change in conformation of the IdoA residue nor α/β interconversion induced substantial changes in the potential energy surfaces of the disaccharide fragments and did not affect the orientation of the glycosidic linkages.

Ensemble average interproton distances for each disaccharide entity were extracted from molecular mechanic calculations and translated into predicted NOEs by a full-matrix relaxation approach; NOEs were then compared with those collected experimentally to verify the reliability of the simulation data (Table 3). The experimentally determined values were in good agreement with the conformations adopted by the disaccharides.

Table 3. Experimentally determined (from T-ROESY experiments) and calculated (from MD and MM calculations) proton–proton distances for the two dermatan sulfate tetrasaccharides, which differ in the anomeric configuration at the reducing end. The notation is A-B-Cα-D (for reducing α-GalNAc) and A-B-Cβ-D′ (for reducing β-GalNAc). Interglycosidic NOEs are in bold. The experimentally determined values were obtained as described in the Experimental Section by applying the isolated spin pair approximation as described.[24]

	Exp. (600 ms ROESY)	MM IdoA in $^1C_4$	IdoA in $^2S_0$	MD β-chair	β-skew
		ΔHexA–A			
A1–A2	2.7	2.51	2.51	2.44	2.43
A1–A3	4.4	4.30	4.30	4.23	4.22
A1–B3	**2.4**	2.28	2.28	2.24	2.23
A4–A3	2.5	2.50	2.50	2.49	2.47
A2–A3	2.6	2.65	2.65	2.59	2.56
		β-GalNAc–B			
B1–B5	2.4	2.40	2.42	2.34	2.36
B1–B3	2.4	2.68	2.63	2.48	2.45
B1–C4	**2.3**	2.26	2.28	2.31	2.31
B2–B4	3.8	3.83	3.81	3.74	3.74
B3–B5	2.3	2.53	2.40	2.33	2.32
B3–B4	2.5	2.45	2.49	2.40	2.42
B4–B5	2.4	2.48	2.50	2.43	2.43
B4–B6	2.5	2.58	2.54	2.88	2.99
		IdoA–Cβ			
$C_\beta1–C_\beta2$	3.1	2.54	3.09	2.51	3.03
$C_\beta1–D′3$	**2.3**	2.47	2.48	2.38	2.38
$C_\beta2–C_\beta3$	2.9	2.59	3.09	2.51	3.03
$C_\beta2–C_\beta5$	2.7	4.04	2.39	3.96	2.29
$C_\beta3–C_\beta4$	2.8	2.57	3.08	2.52	2.94
$C_\beta4–C_\beta5$	2.4	2.50	2.37	2.42	2.35
$C_\beta2–C_\beta4$	3.5	4.31	2.92	4.24	3.00
		β-*red*-GalNAc—D′			
D′1–D′3	2.4	2.50	2.53	2.44	2.45
D′1–D′5	2.4	2.40	2.42	2.40	2.41
D′3–D′5	2.4	2.39	2.40	2.37	2.35
D′4–D′3	2.5	2.45	2.46	2.43	2.42
D′4–D′5	2.5	2.50	2.47	2.43	2.43
D′4–D′6	2.5	3.23	2.56	2.76	2.90
		ΔHexA–A			
A1–A2	2.7	2.51	2.51	2.44	2.44
A1–A3	4.4	4.30	4.30	4.23	4.23
A1–B3	**2.4**	2.28	2.28	2.26	2.25
A4–A3	2.5	2.50	2.50	2.49	2.50
A2–A3	2.6	2.65	2.65	2.58	2.60

and at 36/−54, separated by a low energy barrier (2 kJ mol⁻¹). The $\Phi_{A–B}/\Psi_{A–B}$ glycosidic linkages were centered at about 54/0,

	Exp. (600 ms ROESY)	MM IdoA in $^1C_4$	MM IdoA in $^2S_0$	MD β-chair	MD β-skew
		β-GalNAc–B			
B1–B5	2.4	2.40	2.42	2.35	2.36
B1–B3	2.4	2.68	2.63	2.50	2.47
B1–C4	2.3	2.26	2.28	231	2.31
B2–B4	3.8	3.83	3.81	3.74	3.73
B3–B5	2.3	2.53	2.40	2.34	2.32
B3–B4	2.5	2.45	2.49	2.39	2.42
B4–B5	2.4	2.48	2.50	2.43	2.44
B4–B6	2.5	2.58	2.54	3.18	2.85
		IdoA–C			
C_α1–C_α2	3.0	2.53	3.05	2.51	3.03
C_α1–D3	2.4	2.44	2.40	2.43	2.33
C_α2–C_α3	2.9	2.59	3.09	2.51	3.03
C_α2–C_α5	2.7	4.04	2.39	3.95	2.27
C_α3–C_α4	2.8	2.57	3.08	2.52	2.94
C_α4–C_α5	2.4	2.50	2.37	2.43	2.35
C_α2–C_α4	3.5	4.31	2.92	4.25	3.03
		α-red-GalNAc–D			
D1–D2	2.5	2.42	2.43	2.39	2.39
D2–D3	3.2	3.05	3.05	3.05	3.04
D3–D4	2.5	2.44	2.45	2.42	2.42
D3–D5	2.3	2.33	2.31	2.30	2.34
D4–D6	3.2	3.19	3.13	3.27	3.02
D4–D5	2.7	2.69	2.41	2.69	2.41

Table 3. (Continued)

The conformational space available to the tetrasaccharide was next investigated by MD simulations. Computational models of the four tetrasaccharides were generated by use of the energy minima for each glycosidic junction from the disaccharide energy maps obtained with the MM approach; when two minima were present, the lower in energy was considered. The sulfate groups extended equatorially from each sugar ring. The initial structures were extensively minimized, and trajectory coordinates were sampled every ps; a total of 9000 structures were collected for each simulation. A better representation of the experimentally determined conformer distribution of the four species was obtained by performing a restrained-MD simulation with the AMBER* forcefield and the experimentally derived NOE/J information. Calculations were performed with the GB/SA water solvation model as implemented in MacroModel (MMOD). NOE-derived dihedral angles were included as time-averaged torsion constraints.

The trajectories and the Φ/Ψ scatter plots of the three glycosidic linkages of the β-skew species are displayed in Figure 4. In no cases were chair–skew interconversions of the sugar rings observed. The calculations showed that all glycosidic linkages adopted the *exo* anomeric conformation, in agreement with the MM results and the experimental data. The simulation confirmed the existence, for the two external glycosidic linkages **A**–**B** and **C**–**D**, of a single and rather compact energy located in the same energy region, as indicated by the MM calculations (Figure 4). On the other hand, greater flexibility around the central **B**–**C** glycosidic linkage was evident. Indeed, in the scatter plot of the **B**–**C** glycosidic torsions, the two minima located by the MC calculation belonged to a wide energy valley spanning a larger interval of Φ, Ψ values. Analy-

sis of these data (Table 4) provided other useful information. The averaged values of Φ and Ψ angles reported in Table 4 were in accord with the MM and the MD data, while the standard deviation values were indicative of the degree of flexibility around the glycosidic junction. Starting from the nonreducing end, the average Φ,Ψ values extracted during the restrained MD simulation for the β-skew species were: ΔHexA-GalNAc 50.3/−6.2, IdoA-GalNAc 45.4/−24.5, GalNAc-IdoA 53.6/−0.55 (Table 4 a for the other species). The standard deviation values for both **A**–**B** and **C**–**D** glycosidic linkages were rather low. The central glycosidic linkage appeared to be more flexible, especially along Ψ, as deduced from the higher standard deviation values. Moreover, the average values of both Φ_{B-C} and Ψ_{B-C} torsions diverged from those found by the MM calculations and showed that the two previously located minima belonged to a region spanning a large range of Φ/Ψ torsions. Similar results were obtained for the other species; the conformational behavior was fairly analogous (Table 4 a).

The computational models obtained from the MD were then compared with the experimentally obtained results. Ensemble average interproton distances for each molecule were extracted from dynamic simulations and translated into NOE contacts by a full-matrix relaxation approach. The corresponding average distances obtained for the simulation from $\langle r^{-6} \rangle$ values were compared to those collected experimentally (Table 3). A satisfactory agreement between the calculated and the experimentally determined values was observed. As expected, the deviation of the ring proton distances in residue **C** of α-IdoA from the experimentally derived data was attributable to the equilibrium between $^1C_4$ and $^2S_0$ forms; the smaller deviation of proton distances of both α-skew and β-skew species confirmed the existence of the IdoA residue mainly in the skew conformation (see above). Moreover, a careful study of the simulation data and the corresponding predicted NOEs confirmed the existence of the small NOE contacts of H-1/H-2 **C** with the methyl protons of the *N*-acetyl group located on residue **D** and of H-1/H-2 **A** with the methyl protons of the *N*-acetyl group located on residue **B**, which were all further confirmation of the relative orientations of the sugar rings.

RDC calculation from MD trajectories with TRAMITE

The conformational distribution of the dermatan tetrasaccharide suggested by NOE, MM, and MD studies was further assessed by using RDCs (residual dipolar couplings). The alignment medium for the RDC measurements was a phage solution.[17] RDCs were measured for a natural abundance sample of dermatan tetrasaccharide. In order to obtain $D_{H,H}$ and $D_{C,H}$ RDCs, the measurements of one-bond carbon–proton coupling constants ($^1J_{C,H} + (^1D_{C,H})$) were performed by t_2- and t_1-coupled HSQC experiments (Figure S1 in the Supporting Information). Proton–proton coupling constants ($^3J_{H,H} + (^3D_{H,H})$) were obtained by DQF-COSY and ^1H NMR experiments. $^3D_{H,H}$ values were measured for those signals of good quality that could be unambiguously assigned in both oriented and nonoriented samples. An orientation tensor defining the direction and the magnitude of the alignment of the molecule in the alignment
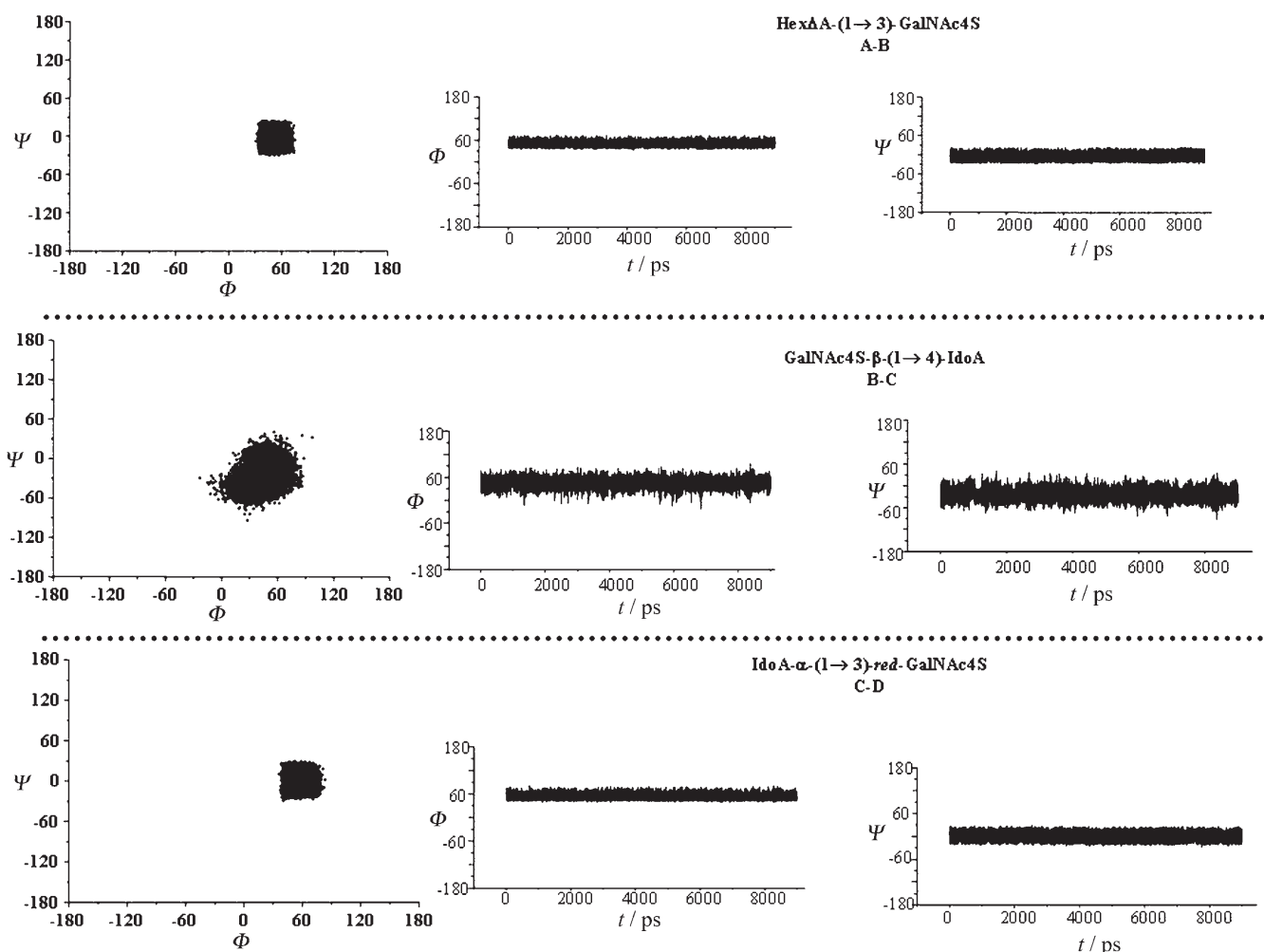
Figure 4. Molecular dynamics trajectories (Φ and Ψ vs. time) and scatter plot of Φ vs. Ψ values, corresponding to the NOE-restrained MD simulation (9 ns) for the tetrasaccharide. The data obtained when the β-skew geometry was employed are shown. All the other simulations produce similar results.

Table 4. The flexibility of the tetrasaccharide. A) Average Φ and Ψ values directly observed from the MD simulation. B) Best-fit average Φ and Ψ values to the RDC data, considering different sets of conformers. The set of conformers that provide the lowest RMSDs are given.					
A)	β-Skew	α-Skew	B)	β-Skew	α-Skew
A-B					
av. Φ	52.8	53.0	av. Φ	50.3 ± 7.6	51.9 ± 7.3
av. Ψ	−1	2.9	av. Ψ	−6.2 ± 11.3	−3.5 ± 11.4
B-C					
av. Φ	47.9	47.6	av. Φ	45.4 ± 13.4	45.4 ± 12.9
av. Ψ	−13.8	−24.4	av. Ψ	−24.5 ± 17.6	−26.6 ± 16.6
C-D					
av. Φ	53.6	53.6	av. Φ	53.6 ± 7.7	52.7 ± 8.2
av. Ψ	−2.9	−1.2	av. Ψ	−0.5 ± 11.9	−6.1 ± 12.0
	β-Chair	α-Chair		β-Chair	α-Chair
A-B					
av. Φ	50.8	52.8	av. Φ	48.2 ± 9.1	47.8 ± 8.5
av. Ψ	2.0	−1.0	av. Ψ	−0.0 ± 9.6	4.13 ± 9.4
	B-C	B-C		B-C	B-C
av. Φ	43.8	43.5	av. Φ	44.2 ± 14.5	43.8 ± 14.5
av. Ψ	−17.7	−20.1	av. Ψ	−22.5 ± 18.8	−25.1 ± 17.9
C-D					
av. Φ	48.6	52.7	av. Φ	48.3 ± 7.8	50.9 ± 6.7
av. Ψ	9.8	14.1	av. Ψ	13.0 ± 8.7	16.3 ± 7.5

medium is required for the interpretation of RDCs. The alignment tensor can be predicted on the basis of the global shape of the molecule, information already encoded in its inertia tensor, which is then used to predict the alignment tensor by the TRAMITE (Tracking Alignment from the Moment of Inertia Tensor)[14] method and then to back-calculate average RDCs from multiple structure files. Calculated RDCs were compared with the experimentally determined ones to evaluate and to refine the consistency of the previously derived conformational behavior.

The instantaneous RDCs associated with every frame saved during the MD simulations predicted with TRAMITE were used, as described above, to derive a linear average of RDCs. The accordance between experimentally determined and calculated RDCs for all the 9000 conformers collected during the simulations is acceptable, as shown by the root-mean-square deviations (rmsd) reported in Table 5. As expected, the deviation from the experimentally determined values is higher for species with the IdoA in the chair conformation, due to their presence in minor amounts in solution.

Table 5. The best fit from the MD simulations to the RDC data. The table compares the RMSD values obtained with TRAMITE when all the computed 9000 conformers from the MD simulations are considered in comparison to the values obtained when a limited subset of conformers is evaluated. The agreement is better in the second case. Nevertheless, the considered 1000 "best-fit" conformers still encompass a certain flexibility around the glycosidic torsion angles and the IdoA ring.

	RMSD (9000 conformers)	RMSD (1000 conformers)
β-skew	0.55	0.35
α-skew	0.50	0.38
β-chair	0.62	0.43
α-chair	0.55	0.43

The agreement between calculated and experimentally determined RDCs was improved when conformers with large RDC deviations were filtered out from the RDC calculations (see RMSDs in Table 5). In the case of the β-skew species, the RMSD decreased from 0.55 to 0.36, and the accordance for the other species was also significantly increased. In each case, a subset of 1000 structures with the lowest RMSDs was considered. These conformers are represented in the Φ versus Ψ maps with gray points (Figure 5).

The average Φ/Ψ values for conformers with the lowest RMSD deviations are reported in Table 4B, and views of the most favored conformers are depicted in Figures 6 and 7. The RDC data substantially confirmed the validity of the data sets
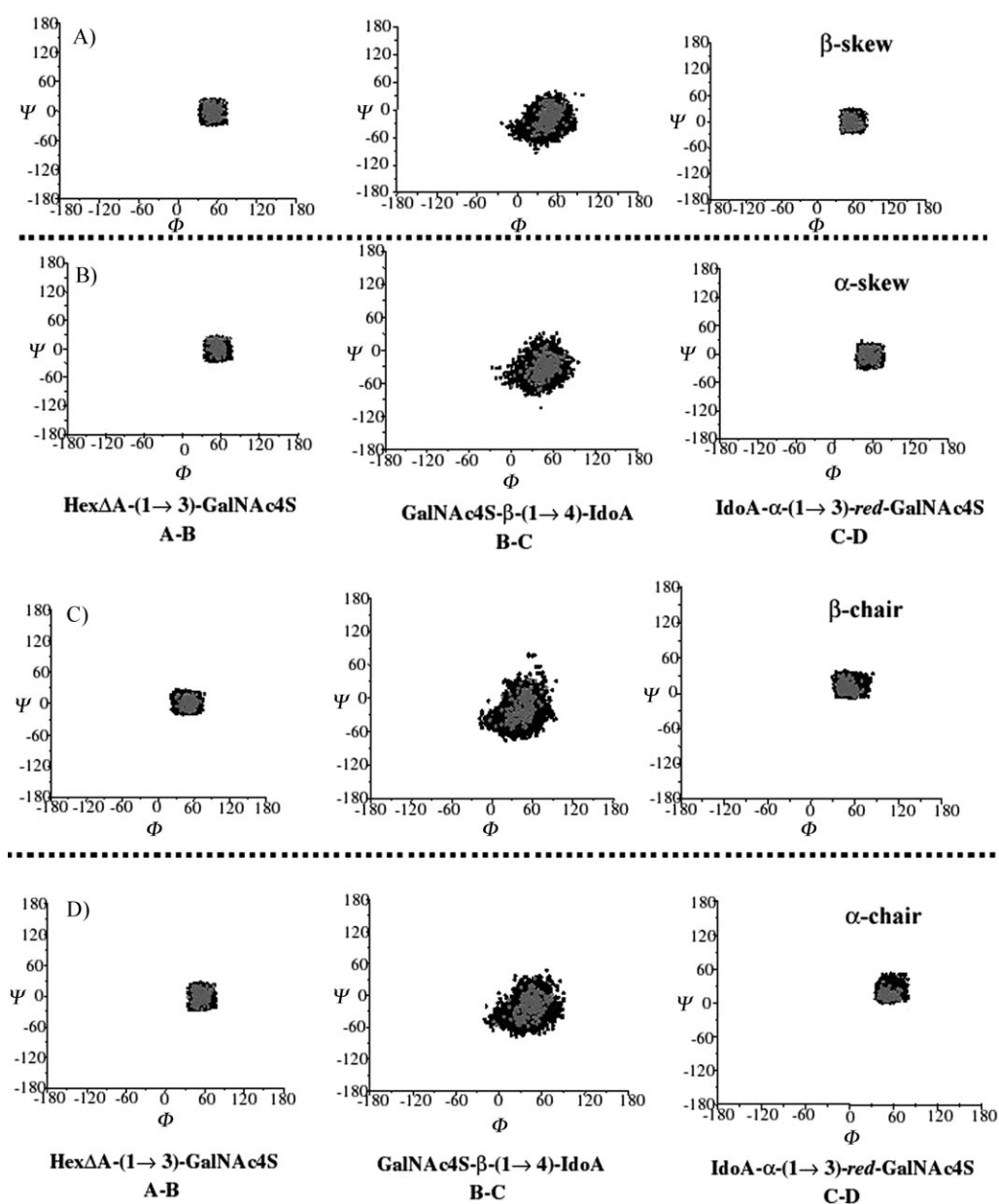
Figure 5. A–D) Scatter plots of Φ vs. Ψ for all the four species (combinations of β/α and skew/chair geometries) making up the dermatan sulfate-derived tetrasaccharide. From top to bottom: β-skew, α-skew, β-chair, and α-chair. The datapoints for the 1000 conformers that give the best fit to the experimentally determined RDC values (those providing the lowest rmsd) are darker. Flexibility is still observable around the glycosidic linkages.

A)

B)
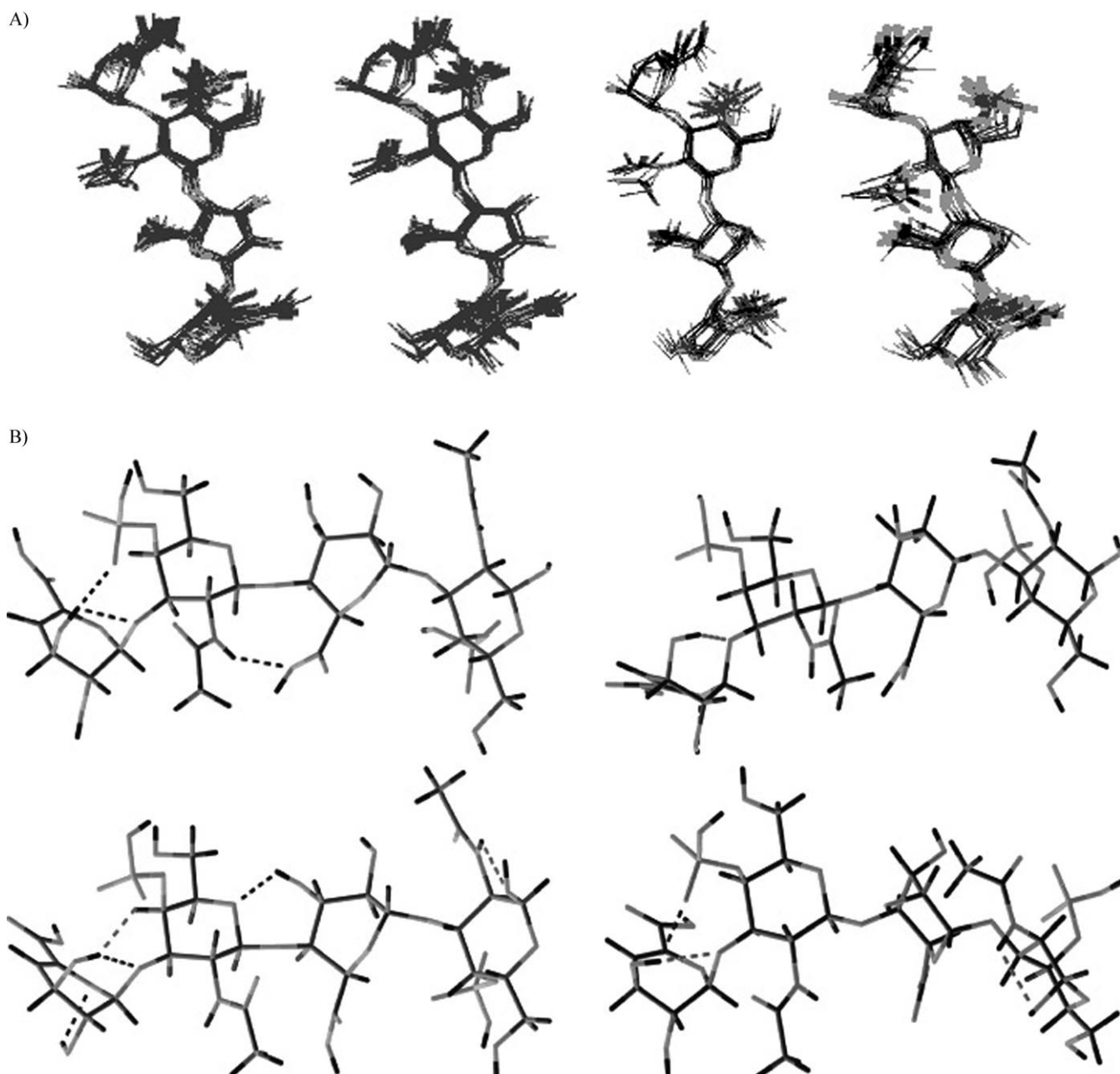
Figure 6. A) Superimpositions of different conformers for each of the four geometries taken from the regions providing the best fit to the experimentally determined RDCs. From left to right: β-skew, α-skew, β-chair, and α-chair. B) Views of the four representative structures (combinations of α/β and skew/chair geometries) from the dermatan tetrasaccharide. In this case, the possible inter- and intraresidue hydrogen bonds are also shown. From left to right and top to bottom: β-skew, β-chair, α-skew, and α-chair.

obtained by the previous NOE-based calculations, though the most favored conformers, represented by the lowest rmsd-calculated RDCs, were distributed in a narrower region of the scatter plot (Figure 5). In fact, the MD data produce a wider distribution of conformers with a substantial flexibility around the glycosidic torsions. In contrast, the best fit between the combined NOE/RDC experimental data with the MD analysis points to more compact regions for the Φ/Ψ torsional maps. In any case, flexibility is required to account for the experimental data, although the actual degree of motion might be a matter of discussion.[18] The glycosidic torsions of the four tet-

rasaccharides showed a similar trend (compare, for each glycosidic torsion, the green points in the four maps in Figure 5), even though rather small but significant differences were detectable (see below for a detailed discussion).

Discussion

The NMR data reflect the existence of four dermatan sulfate-derived tetrasaccharide species, present in different amounts and distinguished by the conformation of the IdoA residue and the anomeric configuration of the free reducing end (β/α
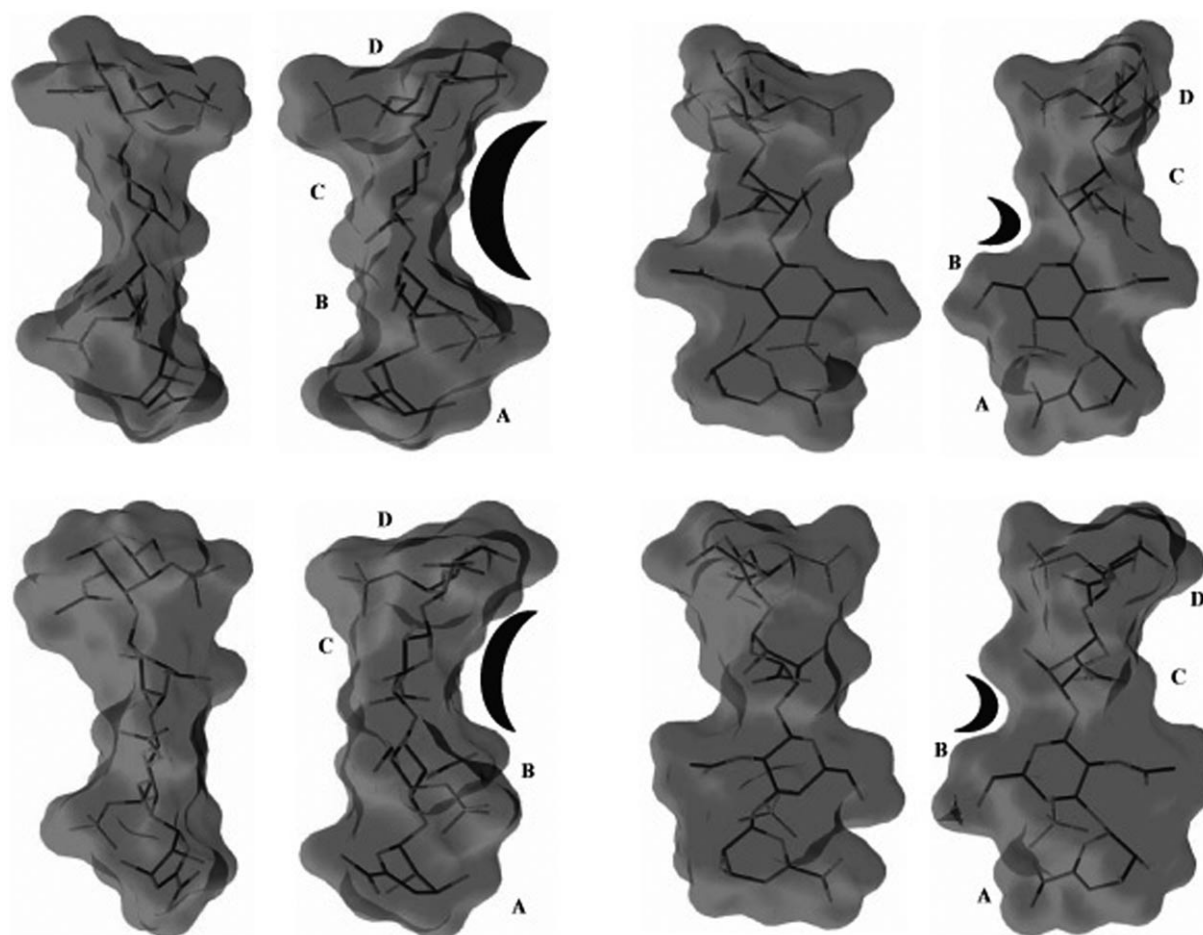
Figure 7. Connelly surfaces of the four major species (combinations of α/β and skew/chair geometries) depicted in Figure 6B. Two different perspectives for each geometry are given. All adopted a similar shape, with different extensions related to the conformation of the IdoA residue. Those with IdoA in $^2S_0$ adopted a more extended shape with a large cleft defined between residues D and B. On the other hand, those with IdoA in the chair conformation presented a smaller but deeper cleft between residues C and B. Three sugar moieties appeared coplanar in the first case (skew), while only two seemed to be coplanar in the second one (chair). Thus, for longer oligosaccharides, a three-residues-per-turn helix-like structure would be present in the first case, while a two-residues-per-turn helix-like structure could appear in the second case. From left to right and top to bottom: β-skew, β-chair, α-skew, and α-chair. Two views are given for each conformer.

in a 1 to 0.6 ratio). Both GalNAc species were present exclusively in the $^4C_1$ conformation. The IdoA species could be present in twisted boat $^2S_0$ and chair $^1C_4$ conformations in approximately 80:20 ratio This observed conformational equilibrium (4:1) adds new data to those previously described for other IdoA residues within GAGs.[4–6, 10–13, 19–22] For instance, within the regular region of heparin, both conformers are almost equally populated with a slight excess of the chair form ($^2S_0/^1C_4$ ~40:60), whereas the presence of a sulfo group at position 3 on the successive glucosamine residue, as in the case of the pentasaccharide with high affinity for AT-III, slightly unbalances the equilibrium towards the skew-boat form ($^2S_0/^1C_4$ ~65:35). The effect of sulfation at position 3 of the adjacent glucosamine is indeed highly dependent on the sulfation of the corresponding IdoA residue, as in the absence of the charged group it leads to an increase in the chair form ($^2S_0/^1C_4$ ~25:75). For 2-O-sulfo IdoA residues, the most dramatic effect takes place when both adjacent glucosamine residues are sulfated at position 3 ($^2S_0/^1C_4$ ~100:0).

The ΔHexA residue, containing a 4,5-unsaturated bond, was present in $^1H_2$ twist boat form, as inferred from the analysis of the $^3J_{H,H}$ coupling constants and also confirmed by the MD simulations that showed the existence of possible internal hydrogen bonds of the hydroxy group HO3 with the glycosidic oxygen O1 and the sulfo group present on the adjacent GalNAc residue **B** (Figure 6).

The combined NOE-based molecular dynamics approach, further improved with the RDC/MD data, allowed an accurate description of the 3D structure of the dermatan sulfate tetrasaccharides through a cautious evaluation of the conformational space effectively available to the species. The RDC calculations substantially confirmed the NOE-based studies and predicted that the most probable structures were located around a well defined region of Φ/Ψ combinations. Furthermore, the data still pointed to a certain flexibility of the central glycosidic linkage. Views of the most favored conformers are depicted in Figures 6 and 7. With respect to the IdoA residue in skew conformation, the RDC-based distribution could be explained in a

straightforward manner. It could be roughly assumed that the glycosidic junctions Φ_{A-B}/Ψ_{A-B} and Φ_{C-D}/Ψ_{C-D} behaved similarly for both α and β anomers. The RDC-based analysis provided less populated regions for both glycosidic angles Φ_{A-B}/Ψ_{A-B} and Φ_{C-D}/Ψ_{C-D}, giving evidence of overestimation of the flexibility of both junctions from the MD data. The major difference, as evident from the scatter plots, is indicated by the behavior of the central linkage (Figure 5 A–B). In the case of the Ψ_{B-C} torsion, in the β anomer (Figure 5 A) most of the conformers with the lowest RMSD were located around $-13.8°$ (Table 4 b) and the distribution of species along the Ψ torsion was almost extended, indicating that this torsion maintained much of the previously found flexibility about the Ψ_{B-C} angle. On the other hand, the flexibility about the Φ_{B-C} torsion (Figure 5 A) was significantly smaller. In the case of the α anomer, the center of the distribution of conformers was shifted to $-24.4°$ and species were distributed around a less extended area of Ψ values (Figure 5 B). In addition, the flexibility along the Φ torsion was restricted. Analogously, species with IdoA adopting a chair conformation, which are present in minor amounts ($<20\%$), were analyzed (Figure 5 C and D). The central torsion **B**–**C** behaved similarly to that described above and appeared to be slightly more flexible. Interestingly, most of the dihedral angles of both **C**–**D** junctions were located in a particular region of the scatter plot (Figure 5).

A distinctive feature of the presence of the skew or the chair conformation is the relative spatial disposition of the two sulfate groups, extending equatorially from the sugar rings. Indeed, the sulfates are oriented on opposite sides with respect to the sugar chain in the skew conformation, whereas in those species with the IdoA residue adopting the chair conformation, the sulfate groups are located perpendicular to each other (Figures 6 and 7). Moreover, as shown in Figure 6 B, several intramolecular hydrogen bonds that could stabilize the structure and be responsible for the folding of the molecules were identified (see also ref. [8]). The surfaces of the four oligosaccharides were built according to the Connelly method to provide additional information regarding the overall shapes of these species (Figure 7). Even though these tetrasaccharides do not adopt a defined secondary motif, it is worth noting that all species adopted a similar shape, with different extensions once again attributable to the conformation of the IdoA residue. Thus, species with IdoA in the $^2S_0$ conformation adopted a more extended shape, as observable from the Connelly surface, in which a large cleft defined between residues **D** and **B**, common to both anomers, was observable (Figure 7), although to different extents. On the other hand, the species with IdoA in the chair conformation presented a more contracted structure, while a smaller but deeper cleft was observable between residues **C** and **B**, with greater folding of the chain with respect to that observed for the skew forms. As demonstrated in Figures 6 B and 7, two sugar moieties appeared coplanar for the α- and β-chair species, while for the α- and β-skew molecules, three sugar residues seemed to be coplanar. Thus, when the saccharide chain were extended to a longer oligosaccharide chain, a two-residues-per-turn helix-like structure would be present in the first case, while a three-resi-

dues-per-turn helix-like structure could appear in the second case.

Conclusions

The locations and the highly charged natures of GAGs explain the mechanical and functional roles of these key molecules. Dermatan sulfate is a GAG found mostly in skin, but also in blood vessels, heart valves, tendons, and lungs. Because of their key roles in a variety of relevant physiological processes and in numerous vital functions within the body, the study of conformational details of a dermatan sulfate-derived oligosaccharide is important for shedding light on its biological role and mechanisms of action at molecular levels. The understanding of the biological roles of such molecules thus requires comprehension of the rules governing their conformational equilibria in solution as a prerequisite toward comprehension of the bioactive conformations of such important glycopolymers.

To this end, we have accomplished the first study of the 3D structure of a dermatan sulfate moiety in solution with the aid of NMR and molecular modeling. Classical NOE-derived conformational analysis has been assisted with an RDC-based approach that yielded a better definition of the conformational behavior of the tetrasaccharide and allowed the consistency of the previous NOE-based results to be checked. The analysis confirmed a moderate flexibility of the two external anomeric torsions, while highlighting a certain degree of flexibility of the central glycosidic linkage.

The IdoA residue can exist in two different conformations that give rise to different distributions of the sulfate groups and also to a different extension of the shape of the molecules. As a consequence, it could be supposed that dermatan sulfate oligo-/polysaccharides might adopt different 3D helices characterized by different numbers of residues per turn, depending on the conformations of the IdoA residues. This conformational flexibility of the IdoA ring between the $^1C_4$ and $^2S_0$ forms might also be evaluated from a biochemical point of view, since this equilibrium could imply a different three-dimensional structure and biological activity of the molecule during recognition processes, as happens in the case of heparin and heparin-derived analogues.[19–22]

Experimental Section

Isolation, purification, and characterization of the dermatan sulfate tetrasaccharide: DS from porcine intestinal mucosa was purchased from Celsus Laboratories (Cincinnati, OH). Chondrointin lyase ABC, 50 munits (Seikagaku Co., Tokyo, Japan) was used to digest DS (30 mg/1 mL) in sodium phosphate buffer (pH 7.0, 150 mM) at 37° for 10 h. The reaction mixtures were heated in a boiling water bath for 10 min to inactivate the enzyme thermally, halting the reaction. The denatured protein was removed by centrifugation at 12 000 g for 10 min. The resulting oligosaccharide mixture was concentrated by rotary evaporation and fractionated by low-pressure GPC on a Bio-Gel P10 (fine) column (4.8×150 cm) with NaCl (0.2 N) mobile phase at a flow rate of 0.5 mL min^{-1} and detection at 232 nm. Each fraction was concentrated by freeze-

drying, desalted by GPC on a Bio-Gel P2 column (4.8×70 cm) with water as the mobile phase and detection at 232 nm, and freeze-dried. The resulting size-fractionated oligosaccharide mixtures were characterized by ESI-MS (Agilent G2445D MSD trap, Agilent Technologies, Inc.). Further purification of DS oligosaccharides was achieved by strong anion-exchange high-pressure liquid chromatography (SAX-HPLC) on a semipreparative SAX S5 Spherisorb column (Waters) with a 0.1–2 M NaCl (pH 3.5) linear gradient elution. The purified fraction were collected, desalted by GPC, and freeze-dried. Purity was determined by analytical SAX-HPLC. ESI-MS was also applied to characterize the purified tetrasaccharide.

NMR spectroscopy: For structural assignments of **OS**, 1D and 2D ^{1}H NMR spectra were recorded with a solution (2 mg) in D$_2$O (0.5 mL), at 300 K and at pD 7, on a Bruker 600 DRX equipped with a cryoprobe. Spectra were calibrated with internal acetone ($\delta_H = 2.225$, $\delta_C = 31.45$).

T-ROESY experiments[23] were recorded with data sets ($t_1 \times t_2$) of 4096×256 points and with mixing times between 200 ms and 700 ms. Interproton distances were obtained by employing the isolated spin pair approximation as described.[24] As usual when T-ROESY experiments are performed, cross-peak intensities were corrected by their corresponding offset effects, according to the actual effective field for each proton resonance in the spectrum. The spin-lock field was attenuated four times (ca. 8000 Hz) with respect to that employed for the hard pulses (ca. 33 000 Hz). Thus, basically only the NOEs involving the methyl groups were affected by offset effects. No correction for Hartmann–Hahn effects was applied, since T-ROESY effectively removes most of these effects. Double quantum-filtered phase-sensitive COSY experiments were performed by using spectral widths either of 3600 in both dimensions or of 2000 Hz in F2 (for coupling measurements), with data sets of 4096×256 points. TOCSY was performed with spin-lock times from 20 to 100 ms, with data sets ($t_1 \times t_2$) of 4096×256 points. In all homonuclear experiments the data matrix was zero-filled in both dimensions to give a matrix of 8k×2k points and was resolution enhanced in both dimensions by a cosine-bell function before Fourier transformation. Coupling constants were determined on a first-order basis from high-resolution 1D spectra or by 2D phase-sensitive DQF-COSY.[25] HSQC and HMBC experiments were measured in the ^{1}H-detected mode by single-quantum coherence with proton decoupling in the ^{13}C domain, with data sets of 2048×256 points. Experiments were carried out in the phase-sensitive mode. A 60 ms delay was used for the evolution of long-range connectivities in the HMBC experiment. In all heteronuclear experiments the data matrix was extended to 2048×1024 points by forward linear prediction extrapolation.

RDC measurements: The isotropic and the aligned solution were prepared by dissolving tetrasaccharide (2 mg) in D$_2$O or D$_2$O resuspended in Pf1 phage as reported previously.[16] The Pf1 phage was purchased from Asla Biotech. According to that company, the Pf1 phage strain LP11–92 is isolated from wild-type *Pseudomonas aeruginosa* and propagated in the phage-free strain LA23–99. The phage is purified on KBr gradient and purchased in a suspension of K-phosphate buffer (pH 7.6, 10 mM), MgCl$_2$ (2 mM), and NaN$_3$ (0.05%, buffer content may be adjusted as to customer needs). Additional data are available.[26] 1D ^{1}H NMR and 2D-DQF COSY spectra were recorded for the measurement of multiple-bond proton–proton RDCs. ^{1}H NMR spectra were recorded with 32k and 64k data points; the H$_2$O signal was saturated in the recovery period of 2 s. No window functions were used for the Fourier transformation. 2D-DQF COSY spectra were acquired with 4096×512 data points in both F_2 and F_1 dimensions. Quadrature indirect dimensions were

achieved through the States-TPPI method.[27] The relaxation delay was 3 s. Spectra were processed by application of a cosine function to both dimensions, and the data matrix was zero-filled by a factor of 2 before Fourier transformation. 2D F_2-coupled HSQC and F_1-coupled HSQC spectra were recorded for the measurement of C—H RDCs. 2D F_2-coupled HSQC spectra were measured with 32k×128 data points, while the FIDs were apodized in both dimensions with a 90° shifted cosine function and zero-filled to give, after Fourier transformation, a 2D spectrum of 32×512. 2D HSQC F_1-coupled HSQC spectra were recorded with 2048k×512 data points, while the FIDs were apodized in both dimensions with a 90° shifted cosine function and zero-filled to give after Fourier transformation a 2D spectrum of 4096×2048. In both cases, the column corresponding to each C—H signal was carefully phased and stored. The sign and the magnitude of RDCs were determined from the difference between the coupling in the oriented and non-oriented sample.[14,18 and references therein] The estimated experimental error is ±0.05–0.1 Hz. The program TRAMITE was freely downloadable at http://desoft03.usc.es/rmnweb/rmnexp_software.html#MD_TRAMITE. For further information, see ref. [14].

Calculations: Molecular mechanics calculations were performed with the AMBER* forcefield as included in MacroModel 8.0. A dielectric constant of 80 was used. Extended nonbonded cut-off distances (a van der Waals cut-off of 8.0 Å and an electrostatic cut-off of 20.0 Å) were used. For each disaccharide structure, both Φ and Ψ were varied incrementally with use of a grid step of 18°, each (Φ, Ψ) point of the map being optimized with 2000 P.R. conjugate gradients. The Molecular Dynamics simulations were run with the AMBER* forcefield; bulk water solvation was simulated by use of the MacroModel generalized Born GB/SA continuum solvent model. All simulations were performed at 300 K, structures were initially subjected to an equilibration time of 300 ps, a 9000 ps molecular dynamic simulation was then performed with a dynamic time-step of 1.5 fs and a bath constant τ of 0.2 ps, and the SHAKE protocol was applied to the hydrogen bonds. Sulfate parameters were adapted as described.[18–19] Trajectory coordinates were sampled every ps, and a total of 9000 structures were collected for every simulation.[28–30]

Ensemble average interproton distances were calculated with the home-made NOEPROM program.[31] Coordinate extractions were performed with the program SuperMap, supplied with the NOE-PROM package, and data were visualized with the ORIGIN program. Solvent-accessible surfaces were calculated with the Surface utility of Macromodel and with the Molecular Surface displays of the Chem3D package.

Acknowledgements

[1] H. E. Bülow, O. Hobe, *Annu. Rev. Cell. Dev. Biol.* **2006**, *22*, 375–407.

[2] I. Capila, R. J. Linhardt, *Angew. Chem.* **2002**, *114*, 426–450; *Angew. Chem. Int. Ed.* **2002**, *41*, 390–412.

[3] R. J. Linhardt, T. Toida, *Acc. Chem. Res.* **2004**, *37*, 431–438.

[4] D. Mikhailov, K. H. Mayo, I. R. Vlahov, T. Toida, A. Pervin, R. J. Linhardt, *Biochem. J.* **1996**, *318*, 93–102.

[5] D. Mikhailov, R. J. Linhardt, K. H. Mayo, *Biochem. J.* **1997**, *328*, 51–61.

[6] B. Mulloy, M. J. Forster, C. Jones, D. B. Davies, *Biochem. J.* **1993**, *293*, 849–858.

[7] V. Blanchard, F. Chevalier, A. Imberty, B. R. Leeflang, Basappa, K. Sugahara, J. P. Kamerling, *Biochemistry* **2007**, *46*, 1167–1175.

[8] A. Almond, J. K. Sheehan, *Glycobiology* **2000**, *10*, 329–338.

[9] K. Pojasek, R. Raman, P. Kiley, G. Venkataraman, R. Sasisekharan, *J. Biol. Chem.* **2002**, *277*, 31179–31186.

[10] G. Gatti, B. Casu, G. Torri, J. R. Vercellotti, *Carbohydr. Res.* **1979**, C3-C7.

[11] D. R. Ferro, A. Provasoli, M. Ragazzi, G. Torri, B. Casu, G. Gatti, J. C. Jacquinet, P. Sinay, M. Petitou, J. Choay, *J. Am. Chem. Soc.* **1986**, *108*, 6773–6778.

[12] D. R. Ferro, A. Provasoli, M. Ragazzi, B. Casu, G. Torri, V. Bossennec, B. Perly, *Carbohydr. Res.* **1990**, *195*, 157–167.

[13] B. Mulloy, M. J. Forster, C. Jones, A. F. Drake, E. A. Johnson, D. B. Davies, *Carbohydr. Res.* **1994**, *255*, 1–26.

[14] H. F. Azurmendi, C. A. Bush, *J. Am. Chem. Soc.* **2002**, *124*, 2426–2427.

[15] I. R. Vlahov, H. G. Bazin, R. J. Linhardt, *Chem. Commun.* **1998**, 1819–1820.

[16] M. R. Hansen, L. Mueller, A. Pardi, *Nat. Struct. Biol.* **1998**, *5*, 1065–1074.

[17] See "Anomeric Effect. Origin and Consequences" (Eds.: W. A. Szarek, D. Horton), *ACS Symp. Ser.* **1979**, *87*.

[18] M. Martín-Pastor, A. Canales, F. Corzana, J. L. Asensio, J. Jiménez-Barbero, *J. Am. Chem. Soc.* **2005**, *127*, 3589–3595.

[19] A. Canales, R. Lozano B. López-Méndez, J. Angulo, R. Ojeda, P. M. Nieto, M. Martín-Lomas, G. Giménez-Gallego, J. Jiménez-Barbero, *FEBS J.* **2006**, *273*, 4716–4727.

[20] J. Angulo, M. Hricovíni, M. Gairi, M. Guerrini, J. L. de Paz, R. Ojeda, M. Martín-Lomas, P. M. Nieto, *Glycobiology* **2005**, *15*, 1008–1015.

[21] N. Jastrebova, M. Vanwildemeersch, A. C. Rapraeger, G. Giménez-Gallego, U. Lindahl, D. Spillmann, *J. Biol. Chem.* **2006**, *281*, 26884–26892.

[22] M. Hricovini, M. Guerrini, A. Bisio, *Eur. J. Biochem.* **1999**, *261*, 789–801.

[23] T. L. Hwang, A. J. Shaka, *J. Am. Chem. Soc.* **1992**, *114*, 3157–3158.

[24] F. Corzana, I. Cuesta, F. Freire, J. Revuelta, A. Bastida, J. Jiménez-Barbero, J. L. Asensio, *J. Am. Chem. Soc.* **2007**, *129*, 2849–2865.

[25] M. Rance, O. W. Sørensen, G. Bodenhausen, G. Wagner, R. R. Ernst, K. Wüthrich, *Biochem. Biophys. Res. Commun.* **1983**, *117*, 479–485.

[26] D. J. States, R. A. Haberkorn, D. J. Ruben, *J. Magn. Reson.* **1982**, *48*, 286–292.

[27] M. R. Hansen, P. Hanson, A. Pardi, *Methods Enzymol.* **2000**, *317*, 220–240.

[28] S. Mari, I. Sánchez-Medina, J. Jimenez-Barbero, A. Bernardi, *Carbohydr. Res.* **2007**, *342*, 1859–1868.

[29] J. L. Asensio, F. J. Canada, X. Cheng, N. Khan, D. R. Mootoo, J. Jimenez-Barbero, *Chem. Eur. J.* **2000**, *6*, 1035–1041.

[30] A. Bernardi, D. Potenza, A. M. Capelli, A. García-Herrero, F. J. Cañada, J. Jiménez-Barbero, *Chem. Eur. J.* **2002**, *8*, 4598–4612.

[31] J. L. Asensio, J. Jiménez-Barbero, *Biopolymers* **1995**, *35*, 55–75.